

Satellite Determination of Stratus Cloud Microphysical Properties

PAQUITA ZUIDEMA* AND DENNIS L. HARTMANN

Department of Atmospheric Sciences, University of Washington, Seattle, Washington

(Manuscript received 30 March 1994, in final form 22 December 1994)

ABSTRACT

Satellite measurements of liquid water path from SSM/I, broadband albedo from ERBE, and cloud characteristics from ISCCP are used to study stratus regions. An average cloud liquid water path of 0.120 ± 0.032 kg m⁻² is derived by dividing the average liquid water path for stratus areas by the fractional area coverage of cloud in the region. The diurnal range in this average cloud liquid water path is about 25%. Stratus cloud liquid water is positively correlated with cloud amount and is negatively correlated with low cloud-top temperature.

Cloud liquid water path (LWP) and cloud albedo measurements are used to derive an effective droplet radius using the plane-parallel cloud albedo model of Slingo. The 2.5° by 2.5° grid boxes are first screened for completely overcast scenes in an attempt to justify the plane-parallel assumption. The mean effective droplet radius for this sample is 10.1 ± 4.4 μm. This serves as an upper bound since small-scale LWP variability is estimated to affect the average albedo by up to 0.07, corresponding to an overestimate in the derived droplet size of up to almost 6 μm. The authors find larger droplet sizes in the evening than in the morning, along with smaller LWPs and lower albedos. No correlation is seen between effective radius and liquid water path, reinforcing the independence of these two parameters. Small droplet sizes are only derived in conjunction with high albedos, but this may simply reflect the effect of LWP inhomogeneity on the albedo and hence the derived droplet size. Individual case studies both support the validity of the methodology given high spatial homogeneity and yet demonstrate the common occurrence of nonhomogeneous conditions within stratus regions.

1. Introduction

Stratus¹ clouds provide about 60% of the total global, annually averaged net cloud radiative forcing, or about 15 W m⁻² net cooling on the radiation balance at the top of the atmosphere (Hartmann et al. 1992). This is explained by the high albedo of stratus clouds relative to the ocean surface and their warm emitting temperatures and their large (24%) global area coverage (Warren et al. 1988). The potentially large impact on climate of changes in stratus clouds has stimulated much recent research. Some research has focused on changes in cloud cover (e.g., Slingo 1990), although changes in the reflectivity of the existing cloud cover from droplet size or liquid water path (LWP) changes may prove to be of equal importance.

Several studies now point to such impacts from microphysical changes. Ship-track effluents, by affecting both the mean droplet size and the total liquid water

amount, provide one demonstrated mechanism for changing cloud albedo (Coakley et al. 1987; Radke et al. 1989). A more theoretical study has hypothesized that increased production of dimethylsulfide (a main source of cloud condensation nuclei (CCN) in clean marine environments) by phytoplankton can lead to a decreased mean particle radius in marine boundary-layer clouds and thereby to increased cloud albedo, given constant liquid water concentration and cloud thickness (Charlson et al. 1987). A model demonstrating the possibility for two stable CCN regimes raises the possibility that the current low-CCN marine regime can shift to a high-CCN regime with its associated higher albedo (Baker and Charlson 1990).

To allow for the modeling of such climate feedbacks, climate modelers increasingly use cloud liquid water as a predictor of cloud optical properties. These simulated liquid water contents, cloud albedos, and droplet sizes then introduce new assumptions about droplet size and liquid water spatial distribution into the models and the way these properties correlate with each other. The parameterizations also tend to be based on surface and aircraft data specific to a few locations and a small spatial scale. Within oceanic stratus regions, the current high quality of satellite microwave data makes possible a reliable, physically direct measure of cloud liquid water that can provide a more appropriate basis for general circulation model stratus cloud pa-

¹ We use the word stratus as a shorthand notation to mean the sum of stratus, stratocumulus, and fog.

* Current affiliation: Program in Atmospheric and Oceanic Sciences, University of Colorado, Boulder, Colorado.

Corresponding author address: Paquita Zuidema, Campus Box 311 c/o PAOS, Boulder, CO, 80309.
E-mail zuidema@monsoon.colorado.edu.

parameterizations. Broadband satellite albedo measurements have long been available, though the large-scale albedo is sensitive to the liquid water path, as well as the spatial distribution of the liquid water and the droplet size. An important consequence of this is that it requires a verification of the radiative transfer modeling assumptions linking large-scale LWPs to their albedos.

To address the large-scale characteristics of cloud liquid water and albedo, we analyzed satellite measurements for the regions and seasons of maximum stratus development throughout a period of two years. The monthly averaged in-cloud LWPs and their climatology are contained in section 3. We then linked the satellite albedo and LWP through a plane-parallel radiative transfer parameterization after screening the data for overcast scenes. This leaves the effective radius as a free parameter with which to make the calculated albedo agree with the observed albedo for the observed LWP. The mean and variations of the inferred effective particle radius provide a consistency check on the calculations. The methodology has been used with some success on data from the First ISCCP (International Satellite Cloud Climatology Project) Regional Experiment, or FIRE (Young et al. 1992; Minnis et al. 1992). For the investigation presented here, we have sought to address the validity of this approach for a larger scale. These results are presented and discussed in section 4. Case studies demonstrating the variation possible between comparisons of satellite-derived LWP and albedo for differing air masses are shown in section 5. The next section describes the data and methodology, including an extensive discussion of the Petty 37-GHz LWP algorithm. This section includes the details of the error analysis.

2. Data, methods, and errors

The ISCCP data (Rossow and Schiffer 1991), in conjunction with the Warren et al. (1988) cloud atlas, defined the overcast stratus regions for study. The Special Sensor Microwave/Imager (SSM/I) satellite data was used to determine cloud liquid water path (Petty 1990). The albedo dataset was supplied by the Earth Radiation Budget Experiment (ERBE), and the radiative parameterization used in this study was developed by Slingo (1989). A sea surface temperature (SST) dataset at 2° by 2° resolution, the Comprehensive Ocean-Atmosphere Data Set (Woodruff et al. 1987), allowed us to investigate the dependence of cloud liquid water path on the SST, and when combined with the cloud top temperature, on a proxy for the boundary-layer depth.

The dataset used in section 4 is more restricted than that of section 3 because it is utilized expressly for a droplet size derivation, while the dataset used in section 3 is meant for the more general purpose of a clima-

tology. The primary dataset used within the droplet size retrieval in section 4 contained all the LWP and ERBE albedo measurements that occurred within two hours of each other and for which the cloud coverage was deemed complete. For a particular region this collocation occurred about once a month and usually lasted a few days. Only those 2.5° by 2.5° grid boxes for which 90% data coverage was available were kept.

Our model's assumption of homogeneous cloud cover required us to successfully identify low overcast stratus clouds. ERBE classifies low overcast clouds as mostly cloudy, for reasons explained in section 2c, and the ERBE scene identification alone cannot ensure that we are only viewing overcast regions. The ISCCP C1 dataset provides a more accurate cloud amount estimate. In the worst-case scenario, however, the ISCCP C1 three-hourly (daylight) data nearest to the SSM/I overpass are gathered five hours before or after the SSM/I overpass time. This raises the possibility that the ISCCP and SSM/I sensors are viewing different cloud fields. Thus, a combination of ERBE and ISCCP information was used to find overcast boxes. Only grid boxes in which every ISCCP pixel was classified as low cloud, and every ERBE pixel was classified as mostly cloudy or overcast, were retained. Although this selection process is crude by necessity, our final selection of 84 grid boxes, or 11% of the total sample, is consistent with frequency distributions of overcast conditions reported elsewhere (Coakley and Kobayashi 1989). The mean cloud-top temperature for this sample is 284 K and ranges from 280 to 290 K, confirming that they are primarily liquid water clouds.

a. Cloud data

The Warren et al. (1988) cloud atlas, compiled from ground-based reports, defined the regions containing high stratus cloud amounts. The advantage is that ground-based observations have an improved view of low clouds. The analysis of ship reports comes from a 30-yr period (1952–1981) and includes the amounts of eight distinct cloud types, as well as of the total cloud, all as a function of season. The spatial resolution is 5° by 5° except in regions with sparse data. We used their cloud-type designation stratus + stratocumulus + fog.

Using the Warren cloud atlas, we selected those geographical regions with a climatological stratus amount of greater than 60% and low amounts of higher clouds (middle clouds < 25%; cirrus < 10%; nimbostratus < 3%) for the analysis in section 3. We used slightly larger areas for section 4 in the hope of capturing a few more collocated ERBE and SSM/I measurements. The three regions will be referred to as the Californian, Peruvian, and Namibian regions.² For the Peruvian and

² While the largest stratus amounts occur in the northern oceans, these regions were excluded because of the presence of precipitation and possible mixed-phase clouds.

Namibian regions, our data span July through November of 1987 and June through November of 1988 and 1989. For the California region, only boreal summer data were used. These locations are given in Table 1.

Table 1 also contains the monthly average ISCCP amounts of low, middle, and high clouds. The ISCCP dataset is at present possibly the best available satellite cloud dataset because of its high resolution and the variety of cloud information available (Rossow et al. 1991). We used ISCCP data to help select regions with only low clouds and to provide a cloud-top temperature. ISCCP uses narrowband spectral radiances from the operational weather satellites, together with atmospheric water vapor and temperature profile data from the Tiros Operational Vertical Sounder (TOVS). After applying a bispectral threshold technique to determine if a pixel is cloudy or clear, ISCCP uses a radiative transfer model to discern cloud information at the 5–8-km pixel size.

Cloud amount is defined as the number of cloudy pixels divided by the total number of pixels. A cloud-top temperature is retrieved from the infrared radiance after the effects of atmospheric water vapor absorption have been removed, and cloud-top pressure is inferred from the TOVS atmospheric temperature profile. The analysis here focuses on clouds with cloud-top pressures greater than 680 mb. The ISCCP pixel data, initially sampled every 30 km, is further summarized at 280-km resolution for every three hours, forming the stage C1 data used in section 4. The monthly summary of the C1 data is the stage C2 data that is used in section 3. The C1 and C2 data state the distribution of the pixels and their mean properties according to classes based on optical thickness and cloud-top pressure. We estimate the error in ISCCP monthly mean cloud amount at 5%, although individual pixels may have larger errors (Rossow and Garder 1993; Wielicki and Parker 1992).

For the analysis in section 3, a random overlap assumption was used to correct the ISCCP low cloud amount for the obscuration caused by upper-level clouds. We used the daytime-only data for the low cloud amount, as nighttime stratus cloud amount retrieval is difficult. We selected only those grid boxes for which the corrected low cloud amount formed at least 70% of the total cloud cover. So doing should not bias our dataset in favor of a particular type of boundary-layer cloud, as clouds above the inversion layer are thought to form by separate processes from the clouds below. The analysis in section 3 used the daily average of ISCCP quantities, except when deriving the diurnal change in cloud LWPs.

b. Liquid water path dataset

We used the SSMI onboard the *F-8* satellite of the Defense Meteorological Satellite Program. The satellite was in a near polar, sun-synchronous orbit, with a swath width of about 1400 km. The ascending equatorial crossings occurred at 0612 local time and the descending equatorial crossings at near 1900 local time. The SSMI had dual-polarization channels at 19.35-, 37.0-, and 85.5-GHz frequencies and a vertical-polarization-only channel at 22.235 GHz. The 85-GHz channel failed in mid-1988 and was not included in our analysis. The pixel size ranges from about 70 km by 45 km for the 19-GHz channels to 37 km by 28 km for the 37-GHz channels. We obtained the data from Remote Sensing Systems Inc. in a format described by Wentz (1991a).

Liquid water droplets emitting unpolarized radiation will diminish the positive brightness temperature difference ΔT_b between the vertically and horizontally polarized radiation emitted by the ocean surface. This forms the physical basis for the Petty liquid water path retrieval (Petty 1990, 1994). The influence of other atmospheric parameters can be factored out by examining a normalized polarization difference P :

TABLE 1. Regions used within section 3.

Region	Location	Season ^a	Average ISCCP low cloud amount ^b	Average ISCCP middle cloud amount ^b	Average ISCCP high cloud amount ^b
Californian	20°–35°N 120°–130°W	JJA	69%	9%	1%
Namibian	10°–20°S 0°–15°E	JJA	66%	6%	3%
Peruvian	5°–20°S 70°–90°W	JJA	69%	15%	1%
Namibian	5°–20°S 5°W–10°E	SON	76%	11%	2%
Peruvian	0°–25°S 70°–90°W	SON	58%	24%	1%

^a SON: September, October, and November; JJA: June, July, and August.

^b 1987, 1988, and 1989 if JJA; 1987 and 1988 if SON. Low cloud-top pressure > 680 mb > middle cloud-top pressure > 440 mb > high cloud-top pressure.

$$P \equiv \frac{\Delta T_b}{\Delta T_{b,\text{clear}}} \\ = \Delta T_b \exp(0.015U + 0.00607WVP - 4.40), \quad (1)$$

where U refers to a wind speed in units of meters per second derived using the Goodberlet algorithm (Goodberlet et al. 1989); WVP is a water vapor path, in units of kilograms per squared meter derived from a statistical algorithm similar to the Alishouse algorithm (Alishouse et al. 1990). The stated accuracy of the wind speed is within 2 m s^{-1} outside of areas containing precipitation, while the water vapor retrieval has a stated accuracy of 2 kg m^{-2} or 0.13WVP , whichever is greater. Petty fitted the clear-sky polarization difference by regressing observed ΔT_b values against retrieved wind speed and water vapor values in a separate cloud-free dataset. Thus, P equals 1 if the pixel contains only clear sky and 0 if the surface is obscured by clouds and rain.

Petty used a closed-form quantitative atmospheric brightness temperature model, neglecting scattering, to show that P at any frequency is well approximated by the effective microwave transmittance τ associated with liquid water alone raised to a power α (about 2) that depends only weakly on other variables:

$$P \approx \tau^\alpha \approx \exp[-\alpha\kappa\text{LWP}/\cos\theta], \quad (2)$$

where LWP is the liquid water path, θ is the SSM/I viewing angle ($\approx 53^\circ$), and κ is the effective mass extinction coefficient of the liquid water. This is determined as a polynomial fit to temperature for each frequency and relies on the index of refraction for water of Ray (1972). Here we assume a cloud temperature of 285 K. The higher-frequency channels are most sensitive to cloud water. For the 37-GHz channel, inverting (2) yields

$$\text{LWP} = -1.42 \ln(P) \text{ in kg m}^{-2}. \quad (3)$$

This algorithm is not valid for precipitating clouds, requiring us to identify and exclude precipitation cases. Some precipitation was flagged through the normalized polarization difference value itself: we took a P value of less than 0.7 to indicate rain. This threshold was chosen based on experience with the Scanning Multichannel Microwave Radiometer (Petty and Katsaros 1990). We found that our results were insensitive to the choice of either 0.8 or 0.7 for P . Although values of P higher than 0.7 may contain rain, the error introduced by underestimating the true extinction coefficient remains small because the total precipitation water mass within stratus clouds remains a small fraction of the total cloud water mass (Petty 1990). Other pixels were excluded if the wind speed and water vapor path values could not be accurately determined. The water vapor path is not strongly sensitive to rain and was only considered inaccurate if the polarization difference

at 19 GHz was less than 24 K. Wind speed values are easily influenced by precipitation, however, and were considered indeterminate if the 19 GHz horizontally polarized brightness temperature was greater than 215 K or if the 37 GHz vertically polarized brightness temperature was greater than 221 K. Pixel footprints overlap at the 19-GHz frequency, and wind speed values of pixels adjacent to flagged pixels were also excluded.

Stratus clouds contain relatively little precipitation. Convective precipitation is suppressed by subsidence from the Hadley cell circulation and by the cool sea surface temperatures, while stratiform precipitation is mostly a light drizzle for which retrieved LWPs are still accurate. In light of this consideration, and because stratus clouds are shallow, ice free, and relatively homogeneous over a large area, stratus clouds provide the best cloud type for this type of study.

Validation of the liquid water path algorithm is difficult because of the lack of surface-truth data. Petty verified the liquid water algorithm on a cloud-free dataset and found a mean liquid water path of zero³ $\pm 0.025 \text{ kg m}^{-2}$, which is smaller than Petty's model-derived error. The Petty algorithm compares well to other physically based algorithms, such as those of Greenwald et al. (1993) and Wentz (1991b). A comparison of 62.5° by 2.5° stratus-region precipitation-free spatial averages yielded mean differences of about $0 \pm 0.0138 (\pm 0.0169) \text{ kg m}^{-2}$ between the Petty and Greenwald (Wentz) retrieved LWPs. Most of the difference can be attributed to varying assumptions about the cloud temperature, and either an inaccurate calculation of the polarization difference existing under clear conditions by the Petty algorithm or an undue influence by surface effects within the Greenwald and Wentz algorithms. In an independent check, Young et al. (1992) compared SSM/I LWP retrievals made using the Petty algorithm to nearly simultaneous surface-based microwave radiometer LWPs. They found a high correlation ($R = 0.97$) and a positive offset of 0.61 kg m^{-2} that can be explained by island contamination of the satellite microwave brightness temperatures.

We set a systematic LWP error of 0.035 kg m^{-2} , or almost 30% for a stratus LWP of 0.130 kg m^{-2} , solely using Petty's model results for an atmosphere with a water vapor path somewhere between 10 and 30 kg m^{-2} and excluding the 85-GHz channel. Though we examined other sources of error, such as spatial variability, varying cloud temperature, drizzle, and uncertainty in the water vapor path value, each contributed errors of not more than 10%.

In summary, the strengths of the Petty LWP algorithm include a strong theoretical foundation, an explicit accounting of surface effects and atmospheric

³ Wherever plus and minus limits are given, these will indicate plus or minus one standard deviation unless otherwise noted.

water vapor, and a predominantly linear response to spatial inhomogeneities. A drawback is that the algorithm will not work if thick but nonprecipitating clouds obscure the surface, preventing a wind speed calculation. The main weakness from this study's point of view, however, is a high sensitivity to precipitation. For this reason, we applied a threshold value to P to exclude rain-containing pixels. For the analysis in section 3, only those bins within which the SSMI sensor did not register any precipitation throughout the entire month formed the final dataset. During an average month this amounted to about one-third to one-half of the total potential number of bins.

c. Albedo data

We used the ERBE S-8 dataset from the ERBS satellite. This satellite is in an orbit with a 57° inclination, which precesses 5° a day relative to the sun so that complete coverage of local time is provided every 36 days. The ERBE experiment and its algorithms are described in Barkstrom and Smith (1986) and Smith et al. (1986). The albedo scanner is broadband, measuring all radiation from 0.2 to $5 \mu\text{m}$. We restricted the viewing zenith angles to not more than 45° , so that the maximum pixel size is about 80 km by 80 km. We excluded pixels with sun angles larger than 72.5° , for which it is difficult to distinguish albedo differences caused by droplet size. Bidirectional functions relate the radiances measured at the spacecraft L to the radiant exitances at the top of the atmosphere M through $M = \pi L/R$, where R is the bidirectional model. These models, given in Suttles et al. (1988), were determined a priori through the ERB instrument flown on *Nimbus-6* and *-7* (Taylor and Stowe 1984, 1986). Similarly derived directional models quantify the dependence of albedo on solar zenith angle for each underlying scene type (Suttles et al. 1988). We have used these to normalize the albedo measurements to a solar zenith angle of 60° .

The models discriminate between four cloud classes: clear (<5% cloud cover), partly cloudy (between 5% and 50% cloud cover), mostly cloudy (between 50% and 95% cloud cover), and overcast (>95% cloudy). The cloud class is chosen by the given pair of shortwave and longwave radiance measurements using a priori statistics (Wielicki and Green 1989). Although the primary purpose is to select the appropriate bidirectional function, a crude measure of the cloud amount is generated. This best approximates the true cloud cover for "average" cloud heights and optical depths and may not be accurate for a region containing only a few specific cloud types. Because the cloud classification algorithm is sensitive to the longwave measurement, scenes overcast with low, relatively warm clouds are often classified as mostly cloudy.

The identification of overcast regions as mostly cloudy regions has implications for the calculated al-

bedo. It is not clear which bidirectional model is more appropriate to apply to our sample⁴; we have used the difference in the two calculated albedos to provide an uncertainty estimate. The fractional difference in albedo⁵ that results if an overcast scene is classified as mostly cloudy is

$$\frac{R_{\text{ov}}}{R_{\text{mc}}} - 1. \quad (4)$$

The magnitude will depend on the sun and satellite viewing geometry that is most likely to occur. For our range of satellite azimuth, satellite zenith, and solar zenith angles, the mean fractional difference is an overestimate of 6.4% of the total albedo, with an uncertainty of 9% about the new mean. Measurements taken near nadir can have differences of up to 15% of the total albedo. The overestimate occurs because overcast cloud fields are more isotropic than mixed cloud and sea surface scenes. A similarly derived difference in the overcast and mostly cloudy directional models can compensate the above overestimate by up to 0.023. In section 4, we will rely on an estimate of the total uncertainty of 10% of the measured ERBE albedo.

d. Albedo parameterization and the validity of the plane-parallel assumption

Two separate parameterizations contribute to the modeled planetary albedo: one to describe the cloud albedo (Slingo 1989) and another to emulate the effects of solar absorption in the atmosphere (Thompson and Barron 1981). The dependence on liquid water path and equivalent radius is explicit in the Slingo parameterization, allowing us to derive an equivalent (also referred to here as effective) droplet size r_e . The Slingo parameterization is strictly valid only for droplet sizes between 4 and $16 \mu\text{m}$ but follows the same functional form for larger droplet sizes.

The planetary albedo for a cloudy sky is determined from Thompson and Barron (1981) as

$$\alpha_{\text{planet}} = a(1 - A_{\text{oz}}) \times \{r_1 S_u + (1 - r_1 S_u)(1 - r_2 A_w) \alpha_{\text{cloud}}\}, \quad (5)$$

where α_{cloud} is the cloud albedo as seen directly above the cloud, $a = 0.95$ accounts for the neglected absorption of the outgoing reflected and scattered radiation, and A_{oz} is the absorption by ozone. Here $r_1 = 0.4$ is

⁴ As pointed out by one of the reviewers, if overcast stratus regions form a large fraction of the sample from which the mostly cloudy bidirectional model is derived, then perhaps this may be the appropriate anisotropic factor to use.

⁵ This is determined as $[\text{albedo}_{\text{mc}} - \text{albedo}_{\text{ov}}]/\text{albedo}_{\text{ov}}$, where the subscripts ov and mc stand for overcast and mostly cloudy, respectively.

the approximate ratio of upward clear-air-scattering above the clouds to that for clear skies, and $r_2 = 0.5$ is the approximate ratio of absorption by water vapor above the clouds to that for clear skies. Term S_u is the fraction of the incident solar radiation that is scattered upward, and A_w is the absorption of the solar radiation by water vapor, both for clear skies. We added to this a surface albedo of 0.07 for the ocean surface and assume a WVP of 20 kg m^{-2} , roughly the mean WVP for our dataset. We estimate an uncertainty in the complete parameterization of about 5% in a planetary albedo of 0.5, mainly caused by uncertainties in A_w , r_2 , and a (and assuming no uncertainty in α_{cloud}).

Aspects of the relationship between α_{planet} , LWP, and effective radius are shown in Fig. 1. The albedo is fairly insensitive to LWP changes for LWPs higher than about 0.120 kg m^{-2} . The albedo is also seen to be more sensitive to droplet size at the smaller droplet sizes. Lastly, because the curves are concave, for a given droplet size the parameterized albedo will always be greater than or equal to the average measured albedo:

$$\overline{\text{albedo}[\text{LWP}]} \leq \text{albedo}[\overline{\text{LWP}}], \quad (6)$$

where $\overline{\text{albedo}[\text{LWP}]}$ corresponds to the mean ERBE albedo measurement, and $\text{albedo}[\overline{\text{LWP}}]$ is the modeled albedo for the mean liquid water path of a grid box.

We made a quantitative estimate of the impact of pixel-scale variations in LWP about the grid-box mean LWP on the grid-box mean albedo. We assumed that the albedo of each LWP pixel is sensitive only to the vertically integrated liquid water contained within that pixel, the so-called independent pixel approximation (Cahalan et al. 1994a). We fitted a Gamma function frequency distribution $\text{freq}(lwp)$ to the data and fitted a curve to the albedo model corresponding to an effective radius of $10 \mu\text{m}$, $\text{albedo}(lwp)$. The average albedo $\langle \text{albedo} \rangle$ is then

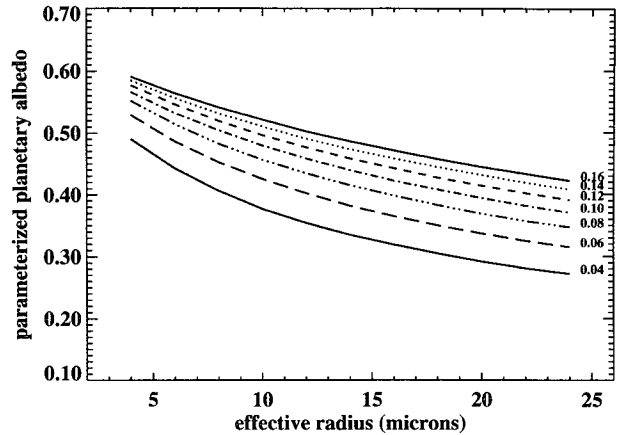


FIG. 2. Parameterized planetary albedo versus effective droplet radii for different liquid water path values in units of kg m^{-2} . (Solar zenith angle: 60° .)

$$\langle \text{albedo} \rangle = \int_0^\infty \text{albedo}(lwp) \text{freq}(lwp) d(lwp). \quad (7)$$

We found a mean estimated correction of only 0.6% in the absolute albedo. Fairall et al. (1990), using surface-based measurements of stratus LWP and albedo, also deduced a small impact on albedo from one-minute variations in a hemispherically averaged LWP.

Similarly, spatial variations in droplet size will slightly increase the measured albedo above the modeled albedo. This can be inferred from Fig. 2, which shows that the planetary albedo is a slightly concave function of droplet size. Stratus droplet radii typically range between 4 and $15 \mu\text{m}$, for which the relationship is substantially more linear than the dependence of the albedo on LWP. The impact of pixel-scale droplet size variations on albedo should then be even less than that calculated above for LWP variability.

Other studies have brought out the importance to the albedo of subpixel variations in LWP (Cahalan et al. 1994b) and in cloud morphology (McKee and Cox 1974; Reynolds et al. 1978; Davies 1984; Welch and Wielicki 1984, hereafter WW; Coakley and Kobayashi 1989; Kobayashi 1993). The influence of a broken cloud geometry is minimized for this study by the near-horizon solar-viewing angle and near-nadir satellite-viewing geometry (Kobayashi 1993). The theoretical study of WW allows for a somewhat more quantitative estimate. If we assume that the effective cloud fraction (the cloud cross-sectional area normal to the sun angle) is unity in their results, then for a cloud fraction of 0.9 (0.7) at overhead sun, the plane-parallel flux will exceed the true reflected flux by less than 10 (25) W m^{-2} (WW, Fig. 12) at a solar zenith angle of 60° . This will reduce our modeled albedo by at most 1.5% (4%).

In contrast, subpixel variations in LWP can substantially influence the average albedo. Cahalan et al.

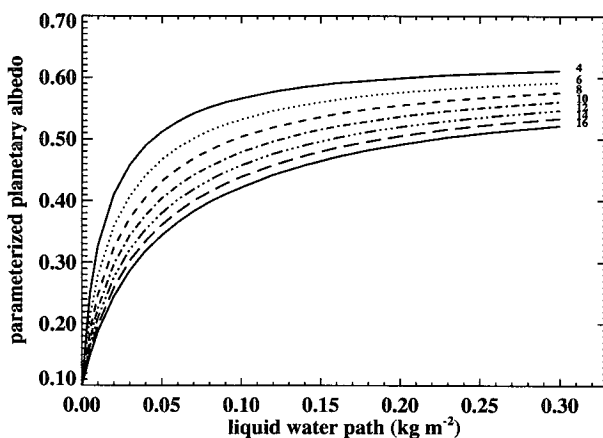


FIG. 1. Parameterized planetary albedo versus liquid water path for different effective droplet radii in units of microns. (Solar zenith angle: 60° .)

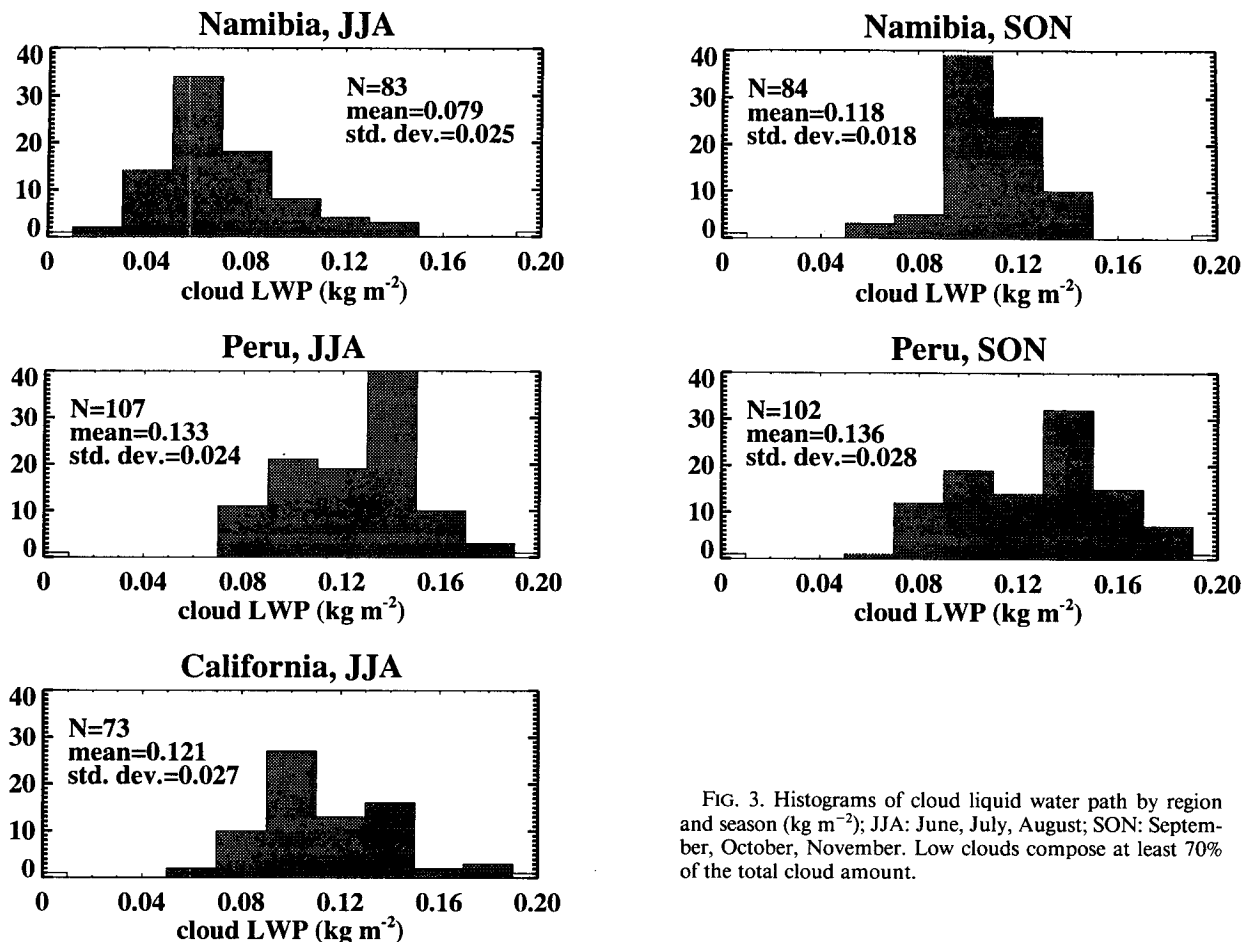


FIG. 3. Histograms of cloud liquid water path by region and season (kg m^{-2}); JJA: June, July, August; SON: September, October, November. Low clouds compose at least 70% of the total cloud amount.

(1994b) applied a fractal model fit to variations in one-minute averages of LWP⁶ sampled over 18 days during FIRE after excluding cloud-free samples and found a decrease in the absolute albedo of about 0.07 for our range of solar zenith angles (their Fig. 6). The large-scale LWP variability effect we calculated previously is thus only one contributor to the total effect. Evaluating the impact of subpixel LWP variations is beyond the scope of this study, but the results of Cahalan et al. (1994b) suggest that we cannot ignore it.

Likewise, variations in droplet size occurring at scales larger than the photon mean free path but less than the ERBE pixel size could also impact albedo. Some evidence exists, for example, that cloud edges may be composed of smaller drops than cloud centers (Coakley 1991). To date no measurements are available of the dependence of effective droplet size on scale. Unless

droplet size variability is far greater than that of LWP, this effect remains subordinate to that caused by LWP variability.

3. Cloud liquid water paths

Monthly averages of the LWP derived from all the (ISCCP) cloudy pixels were determined as follows. We divided the monthly mean LWP value by the ISCCP C2 total cloud amount for each 2.5° by 2.5° region previously determined to contain mostly low clouds, as outlined in section 2a. This derived monthly mean cloud LWP is independent of cloud amount (we will use the term "cloud LWP" to distinguish this quantity from a simple LWP average over an entire region). We estimate an upper limit of 5% to the errors in the cloud LWP caused by errors in the cloud amount. We examined the diurnal cycle of cloud LWP and correlated cloud LWP to cloud amount, sea surface temperature (SST), low cloud-top temperature (CTT), and the difference between the SST and the CTT, referred

⁶ These averages, in contrast to those used by Fairall et al. (1990), relied on a narrowbeam instrument.

to here as S . Term S can serve as a proxy for the boundary-layer depth if one assumes a near-constant boundary lapse rate. A comparison of ISCCP monthly mean cloud-top temperatures to cloud-top temperatures derived from GOES data using a hybrid bispectral method (Minnis et al. 1992) revealed that the ISCCP values are 5 K warmer in the mean but that the spatial patterns matched reasonably well (S. Klein 1994, personal communication).

Figure 3 contains histograms of the cloud LWP by region and season, along with their respective means and standard deviations. The overall mean cloud LWP, for this data sample, is $0.120 \text{ kg m}^{-2} \pm 0.032 \text{ kg m}^{-2}$. From Fig. 1 we see that this average cloud liquid water falls in the region where cloud albedo is sensitive to cloud droplet size but relatively insensitive to further increases in LWP. The Namibian stratus region shows a strong seasonal cycle with greater cloud LWP in autumn (SON) than in summer (JJA), whereas the Peruvian region does not. The Peruvian region had much higher cloud LWPs

in 1988 (mean = 0.142 kg m^{-2}) than in 1987 (mean = 0.121 kg m^{-2}) (not shown in Fig. 3), coinciding with warm SST anomalies in mid-1987 and cold SST anomalies in 1988.

Figure 4 contains histograms of the total cloud amount for each region and season, while Fig. 5 is a scatterplot of cloud LWP versus total cloud amount, with symbols indicating the region and season. Figure 5 shows a significant but weak positive correlation between cloud LWP and cloud amount. This is mirrored in the differences between the mean values for each region and season. The June, July, and August season in the Namibian region has the lowest cloud LWPs and also the lowest mean cloud amount of any of the regions and seasons. The Namibian region shows a large boreal summer-to-fall change in both cloud LWP and in cloud amount (from 77% to 89% mean cloud amount), whereas the Peruvian region has negligible seasonal variation in either. An interesting exception is the interannual change in the Peruvian region, which showed only a slight increase of 2.5% in mean low

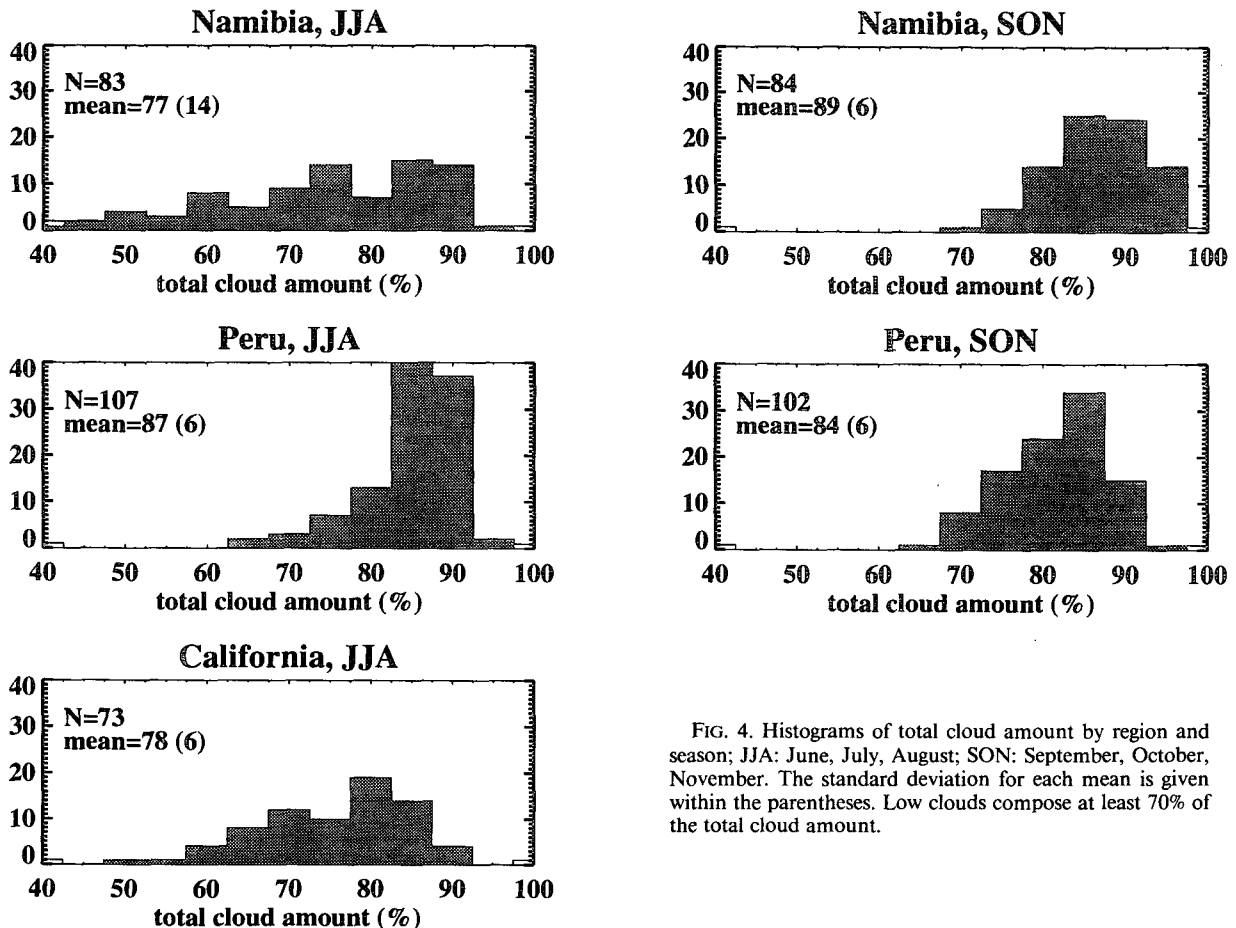


FIG. 4. Histograms of total cloud amount by region and season; JJA: June, July, August; SON: September, October, November. The standard deviation for each mean is given within the parentheses. Low clouds compose at least 70% of the total cloud amount.

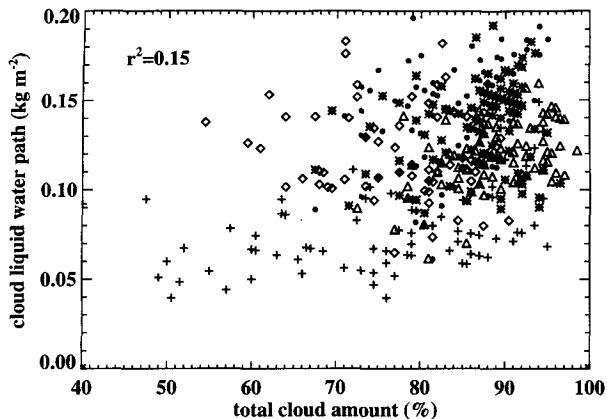


FIG. 5. Cloud liquid water path versus total cloud amount: + refers to the Namibian summer, * to the Peruvian summer, the triangle to the Namibian fall, the diamond to the Peruvian fall, and the dot to the Californian region. Low clouds compose at least 70% of the total cloud amount.

cloud amount from 1987 to 1988, whereas cloud LWP's increased by over 15%.

The dawn/dusk SSMI orbit permits a two-point sampling of the stratus diurnal cycle. Though stratus cloud amount is known to peak in the morning (e.g., Minnis and Harrison 1984; Heck et al. 1990), the accompanying large-scale daily changes in cloud liquid water are not as clearly documented. The SSMI samples these regions between 0500 and 0700 (1700 and 1900) local time, coincident with or slightly lagged to the maxima (minima) in the daily cloud amounts, respectively. The cloud LWP diurnal cycle may not correspond exactly to the cloud amount diurnal cycle (e.g., Heck et al. 1990; Minnis et al. 1992), but the two cycles are probably near each other. Table 2 describes the morning and evening mean cloud LWP's, along with their respective low cloud amounts. The largest diurnal change in cloud liquid water occur in Namibia and Peru during their seasons of maximum stratus development. A slight diurnal cycle in mean cloud-top temperature was evident in the ISCCP dataset also, with colder temperatures occurring in the morning.

a. Dependence of cloud LWP on SST, cloud-top temperature, static stability

Previous studies have shown a strong negative correlation between seasonal subtropical marine stratus cloud amount and seasonal-mean SST (Hanson 1991; Oreopoulos and Davies 1992). However, the seasonal changes in low cloud amount correlate better to variations in lower-tropospheric static stability than in SST (Klein and Hartmann 1993). It is likely that cloud LWP, because it is related to cloud amount in our interregional, seasonal, and diurnal comparison, also depends on these variables. We found the same relationships to hold for each of the regions, as well as similar ranges in SST and low CTT values for each region, and in Fig. 6 we show only the analysis for all of the data combined. The mean low CTT for the combined dataset is 286 K, close to Petty's LWP algorithm choice of 285 K, and the mean value for S is $6.9^\circ \pm 1.5^\circ\text{C}$. As shown in Fig. 6, cloud LWP is most strongly correlated to low CTT (correlation coefficient $r = -0.50$) rather than to either SST ($r = -0.17$) or S ($r = 0.36$). The highest LWP's occur at low CTT, low SST, and a high value for S . The low correlation between cloud LWP and S may be in part due to the large expected error in instantaneous values of S . The LWP-CTT correlation is higher for the Namibian and Californian regions, with explained variances of 31% and 42%, respectively, possibly because they were less contaminated by middle and high clouds than the Peruvian data sample.

Regional differences in cloud LWP mirrored the same relationships to SST, CTT, and S . The Peruvian region's higher cloud LWP average, when compared to the Namibian region (0.135 kg m^{-2} versus 0.099 kg m^{-2}), corresponded to a lower average CTT (285.3 K versus 286.8 K) and a larger S (7.4° versus 6.5°C). Summer to fall variation in cloud LWP was anticorrelated to CTT in Namibian stratus (explained variance of 52%). In the Peruvian region, much higher cloud LWP's in 1988 were associated with the ENSO-affected decrease in mean SST (explained variance of 59%). This corresponds to a $\delta\text{LWP}/\delta\text{SST}$ of $-0.01 \text{ (kg m}^{-2})/^\circ\text{C} \pm 0.005$, or almost an 8% decrease in cloud LWP from the mean with a rise in SST of 1°C .

TABLE 2. Diurnal cycle in cloud liquid water path, derived from SSMI data.

Region/season	Morning cloud LWP ^a (kg m ⁻²)	Evening cloud LWP ^a (kg m ⁻²)	AM/PM difference (kg m ⁻²)
California/JJA	0.130 (0700, 70.3)	0.108 (1600, 63.3)	0.022 ± 0.023
Namibia/JJA	0.094 (0900, 70.8)	0.069 (1500, 62.5)	0.025 ± 0.023
Peru/JJA	0.157 (0900, 6.2)	0.119 (1500, 72.5)	0.038 ± 0.029
Namibia/SON	0.140 (0900, 81.1)	0.098 (1500, 75.3)	0.042 ± 0.019
Peru/SON	0.155 (0900, 70.1)	0.117 (1500, 64.0)	0.038 ± 0.033

^a Local time and its low cloud amount is given within parentheses. Low clouds compose at least 70% of the total cloud amount.

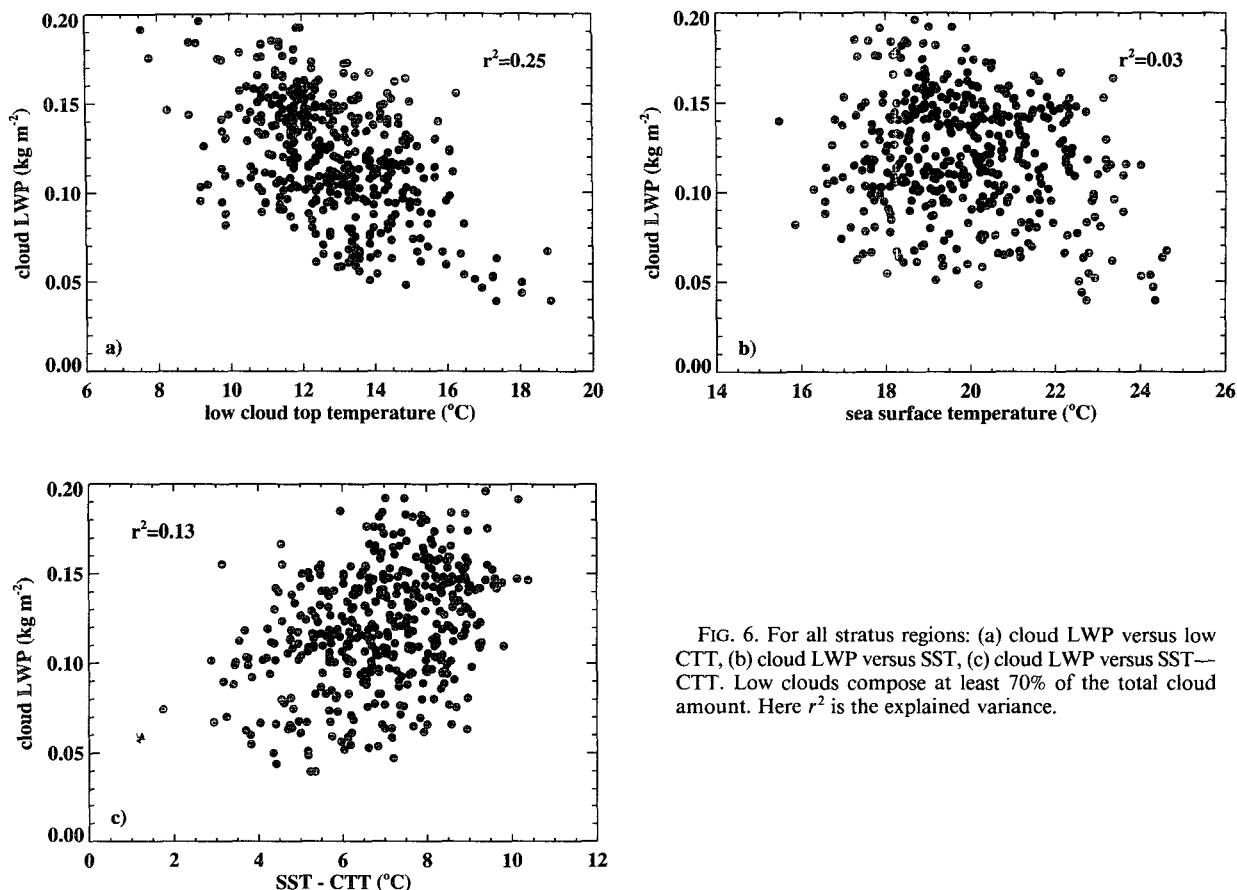


FIG. 6. For all stratus regions: (a) cloud LWP versus low CTT, (b) cloud LWP versus SST, (c) cloud LWP versus SST—CTT. Low clouds compose at least 70% of the total cloud amount. Here r^2 is the explained variance.

These correlations are consistent with the cloud top rising as the cloud LWP builds. Cloud-top temperature depends not only on the SST but also on the inversion height and subsidence rate, so its strong correlation to cloud LWP is not surprising. Studies of the stratus diurnal cycle have reached similar conclusions using satellite inferences (Minnis and Harrison 1984) and aircraft observations (Betts 1990; Hignett 1991; Minnis et al. 1992). These studies also show that cloud-base heights undergo an opposite diurnal cycle, with base heights rising during the day and lowering during the night. However, cloud-base heights vary little interregionally and interseasonally (Warren et al. 1988). Relatively constant cloud-base levels mean that S can be taken as a measure of the cloud thickness, explaining its positive correlation to cloud LWP.

4. Effective droplet radius

The primary dataset of instantaneous, collocated LWP, and albedo measurements had a mean LWP of $0.140 \text{ kg m}^{-2} \pm 0.052 \text{ kg m}^{-2}$ and a mean albedo of 0.506 ± 0.052 . The larger LWP, as compared to the average cloud LWP derived in section 3, comes about

because we selected only completely overcast 2.5° by 2.5° regions. Consistent with the results of section 3, regions with mean cloud amounts of 100% have higher cloud LWPs. To arrive at a unique value for the effec-

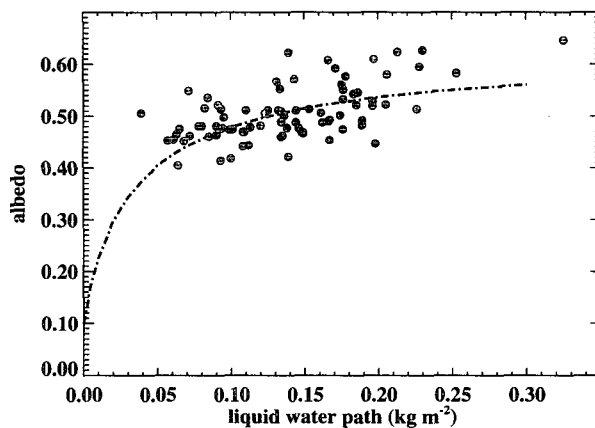


FIG. 7. Parameterized fit and observations of albedo versus LWP for the overcast stratus regions. The albedo parameterization for an effective radius of $10 \mu\text{m}$ is shown by the dot-dash line. $N = 84$.

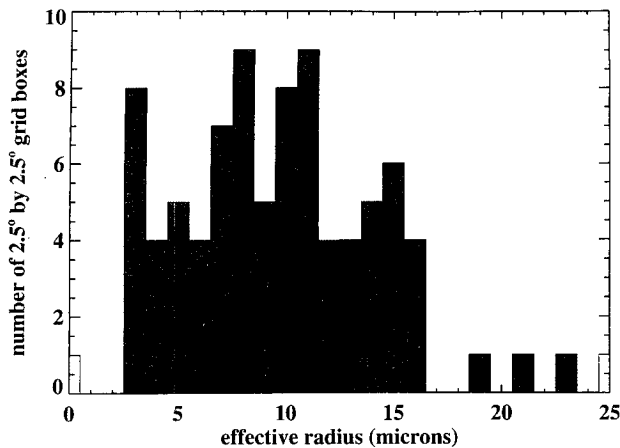


FIG. 8. Histogram of the derived effective radius for overcast stratus regions. Mean effective radius: $10.1 \mu\text{m} \pm 4.4 \mu\text{m}$.

tive radius of each LWP and albedo pair, we inserted the LWP value into the parameterized albedo and iterated the effective radius until the modeled albedo value agreed with the measured ERBE albedo. We constrained the effective radius to not be less than $3.5 \mu\text{m}$, below which the Slingo parameterization becomes multivalued.

Figure 7 contains a scatterplot of the albedo versus liquid water path measurements for the overcast stratus regions and the parameterized albedo–LWP relationship for an effective radius of $10 \mu\text{m}$. The data show considerable scatter. The fit made using the Slingo parameterization can explain about 28% of the variance within the observations. Figure 8 shows the derived effective radii for each measured LWP–albedo pair in the form of a histogram; the mean radius is $10.1 \mu\text{m} \pm 4.4 \mu\text{m}$.

The effective radii derived using this method are more sensitive to the albedo measurements than to the LWP measurements. As shown in Fig. 9a, no correlation exists between the effective radius and liquid water path beyond, initially, a slight increase in the radius with the LWP. The albedo, however, is well correlated to the effective radius (Fig. 9b). High albedos occur only in conjunction with small droplet sizes. We find a larger mean effective radius in the evening ($12.1 \mu\text{m}$) than in the morning ($8.8 \mu\text{m}$), which is accounted for by the lower mean evening albedo of 0.48 as compared to the mean morning albedo of 0.52. Although the mean LWP is larger in the morning (0.149 kg m^{-2}) than in the evening (0.128 kg m^{-2}), this is not enough to explain the change in albedo, and a substantial change in effective radius is implied.

The effective radius calculations were repeated for worst-case scenarios in which the total errors in LWP and albedo were assumed to conspire to give over- and underestimates of effective radius. These upper and lower bounds on r_e are displayed in Fig. 10. The range afforded by these cumulative uncertainties is quite large, with a difference between the mean minimum and maximum radii of about $18 \mu\text{m}$. Table 3 lists possible sources of error and their effect on the derived droplet size. Errors in albedo, though smaller than the LWP uncertainties, have a more pronounced influence on the derivation of the droplet radius.

We performed sensitivity tests of the derived droplet size to the choice of ERBE bidirectional model and to the plane-parallel assumption. By invoking the ERBE mostly cloudy bidirectional model rather than the overcast bidirectional model, we find a new mean effective radius of $10.3 \mu\text{m}$. If we estimate that an accounting of subpixel LWP variability will diminish each modeled albedo by 0.07 (0.05), consistent with the findings of Cahalan et al. (1994b), we derive a new

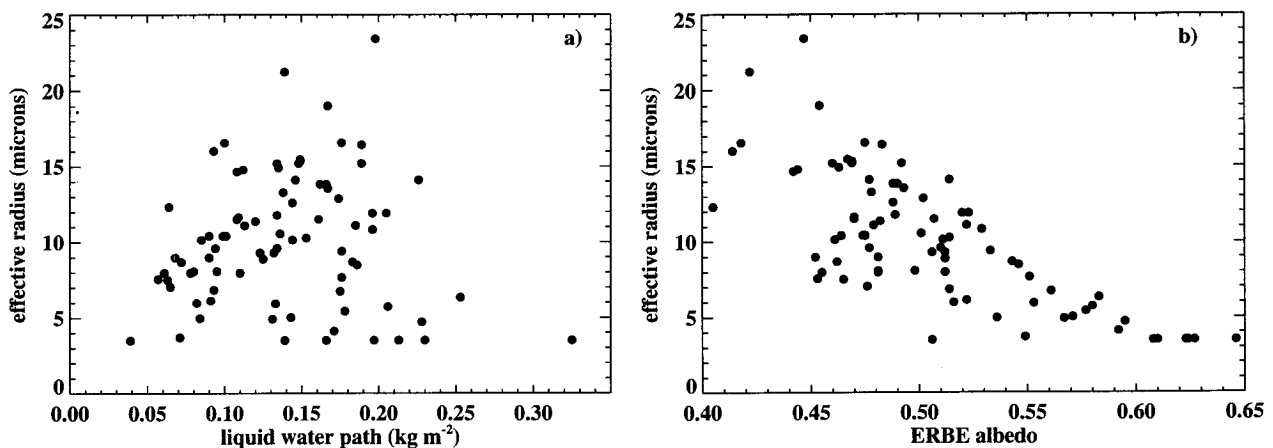


FIG. 9. For all overcast stratus regions: (a) the derived effective radius versus liquid water path and (b) the derived effective radius versus the measured albedo.

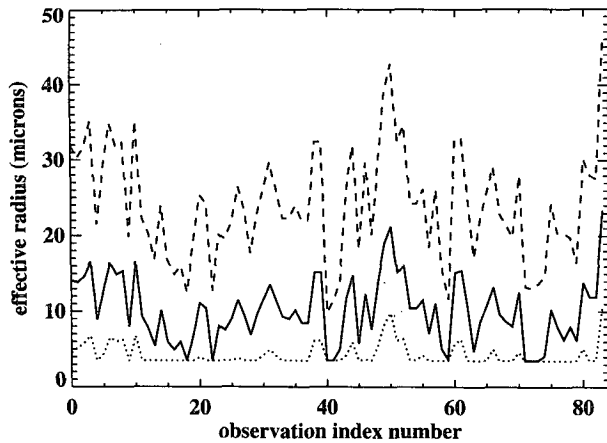


FIG. 10. Maximum (dashed line), minimum (dotted line), and unaltered (plain line) effective radius for each liquid water path-albedo pair. The mean maximum radius is $24 \pm 7 \mu\text{m}$, and mean minimum radius is $4 \pm 1.5 \mu\text{m}$. An LWP error of 0.035 kg m^{-2} , a measured albedo error of 10% of the total albedo, and an error in the albedo model of 5% are assumed.

mean droplet size of $4.4 (5.0) \mu\text{m}$. This will serve as a crude estimate, as Cahalan et al. (1994b) found that large LWPs are more spatially variable than small LWPs.

a. Discussion

There are inherent difficulties in making comparisons between the droplet sizes derived here and those found elsewhere. Our derived droplet size applies to an entire 2.5° by 2.5° region and is not directly comparable to in situ measurements for which droplet sizes can change dramatically on small spatial scales (Nakajima et al. 1991). While aircraft may be taking data anywhere within the cloud, the ERBE shortwave sensor is mainly responding to the upper 20% of the cloud where the drops tend to be larger (Nakajima et al. 1991). Our sample is also not representative of all stratus clouds, as the high mean liquid water path may correspond to atypical droplet spectrums.

Yet, the mean derived effective radius is in general accord with other studies, lending credibility to the methodology employed here. Most aircraft measurements within stratus regions have found effective radii ranging between 4 and $8 \mu\text{m}$ for nondrizzling stratus and between 7 and $18 \mu\text{m}$ in drizzling stratus (Nakajima et al. 1991; Duda et al. 1989; Jensen 1990; Rawlins and Foot 1990). In a study similar to this one, Minnis et al. (1992) found general agreement between a microwave-derived and shortwave-derived LWP, assuming an effective radius of $8 \mu\text{m}$.

A derived effective radius that is larger in the evening than in the morning is consistent the results of another satellite study of droplet sizes (Han et al. 1994) done

using a different technique. Though Minnis et al. (1992) found larger drops in the morning rather than in the evening during FIRE, this appears to reflect a site-specific continental influence (Han et al. 1994). Luo et al. (1994), applying yet another satellite-retrieval method, calculated slightly larger drops at 0230 local time than at 1430 within Peruvian stratus, neither contradicting nor supporting our findings. Cahalan et al. (1994b) found that the higher morning LWP is associated with increased LWP variability. This effect implies a greater reduction in the value of the mean morning effective radius than in the mean evening droplet radius, reinforcing the diurnal cycle we find here.

Models that parameterize drizzle as a function of LWP, following Nicholls (1987), can find increased amounts of drizzle present in the morning (e.g., Bretherton 1990). This would suggest that the effective radius should be larger in the morning than in the evening, contrary to our results. Our sample may simply not contain enough drizzle to have a significant impact on our results. Drizzle concentrations are generally low, and small effective radii have been measured even when drizzle is present (e.g., King et al. 1990). At present no observational evidence exists of such a drizzle diurnal cycle, however, and it may be that a parameterization of drizzle based solely on the LWP is not sufficient.

We sought an explanation for the diurnal cycle of the effective radius. It may be that our observed droplet size reflects a differing sampling of the morning and evening mean values. Our evening sample is smaller than our morning sample (29 bins versus 55 bins) because overcast conditions are more common in the morning than in the evening. Cloud decks that remain overcast by evening may be those that contain larger drops in the morning than the mean of the clouds forming our morning composite. Yet larger drops are more likely to form drizzle, absorb more shortwave radiation, and allow the radiation to permeate deeper into the cloud (Wiscombe et al. 1984). As a result, morning clouds with extraordinarily large drops are more likely than the general population to warm the subcloud layer, be cut off from the surface moisture flux, and dissipate. While we cannot completely ignore the impact of the sampling, the increased solar ab-

TABLE 3. Parameter uncertainties.

Parameter	Parameter uncertainty	r_e Uncertainty ^a
LWP (section 2b)	0.04 kg m^{-2} (40%) ^a	$3 \mu\text{m}$
ERBE albedo (section 2c)	10% (0.05) ^a	$4 \mu\text{m}$
Planetary albedo parameterization (section d)	5% (0.025) ^a	$3 \mu\text{m}$

^a Evaluated at mean LWP and albedo values.

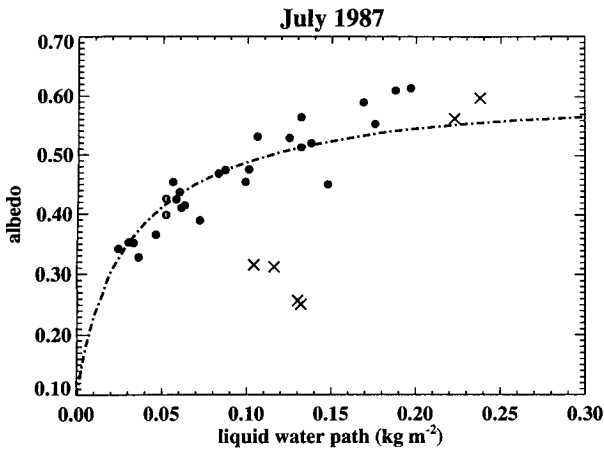


FIG. 11. ERBE albedo versus LWP, California region, for July 1987. \times corresponds to grid boxes containing one or more pixels with normalized polarization differences (P) between 0.7 and 0.8. Dot-dashed line is the Slingo-parameterized albedo for an effective radius of $9.3 \mu\text{m}$.

sorption and likelihood of precipitation will diminish the importance of this effect.

Another explanation presents itself in the following picture of the diurnal evolution of a stratus cloud. The thick morning clouds absorb shortwave radiation throughout the day (Stephens 1984) and entrain dry air from above the cloud top (Nicholls 1984). Shortwave absorption can warm the cloud layer enough to introduce a subcloud temperature discontinuity that discourages the upward mixing of moisture into the cloud. Cloud-top entrainment of warm, dry air then dominates, and the cloud at least partially dissipates (Rogers and Olsen 1990). This leads to a reduced liquid water path and a decreased droplet number density that encourages droplet sizes to grow. The larger droplet sizes derived in conjunction with lower evening albedos (and hence smaller optical thickness) may thus be genuine.

The independent variations of LWPs and droplet sizes (Fig. 9a) seen here corroborate similar results from the cloud composite studied by Nakajima et al. (1991) and from arctic stratus clouds (Herman and Curry 1984). The lack of correlation must reflect variations in either cloud thickness or surface-averaged droplet radius. The observed relationship between the albedo and the droplet size in Fig. 9b can be explained either by true droplet size variations or by small-scale LWP inhomogeneities. High albedos can indicate homogeneous cloud cover as well as small droplet sizes, whereas low albedos can be caused either by deviations from plane-parallel homogeneity or by larger drops. The LWP-variability overestimate is greater at higher LWPs (albedos), strengthening the apparent r_e -albedo relationship. Since the impact of small-scale LWP vari-

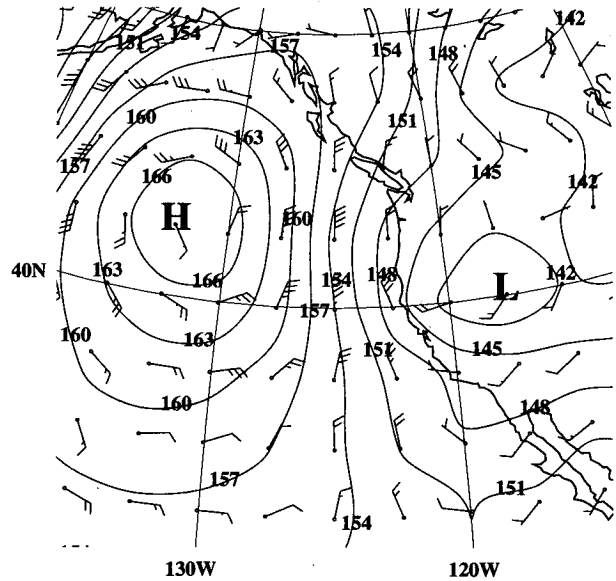


FIG. 12. The 0000 UTC 17 July (1600 local time) 1987 850-mb geopotential heights (dekameters) and wind vectors (m s^{-1}).

ability is embedded within the droplet size derivation, the two effects cannot be separated.

5. Case studies: July and August 1987

The results from the previous section relied on the selection of large, completely overcast regions. Such a best-case dataset allowed us to establish that the meth-

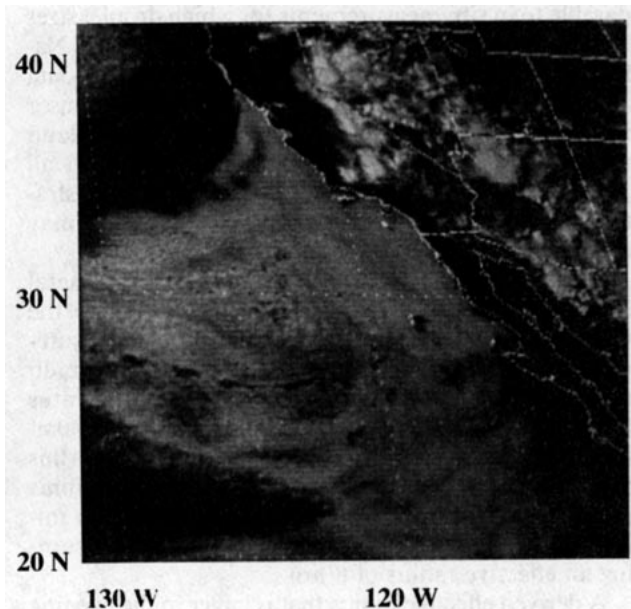


FIG. 13. GOES visible image for 0000 UTC 16 July (1600 local time).

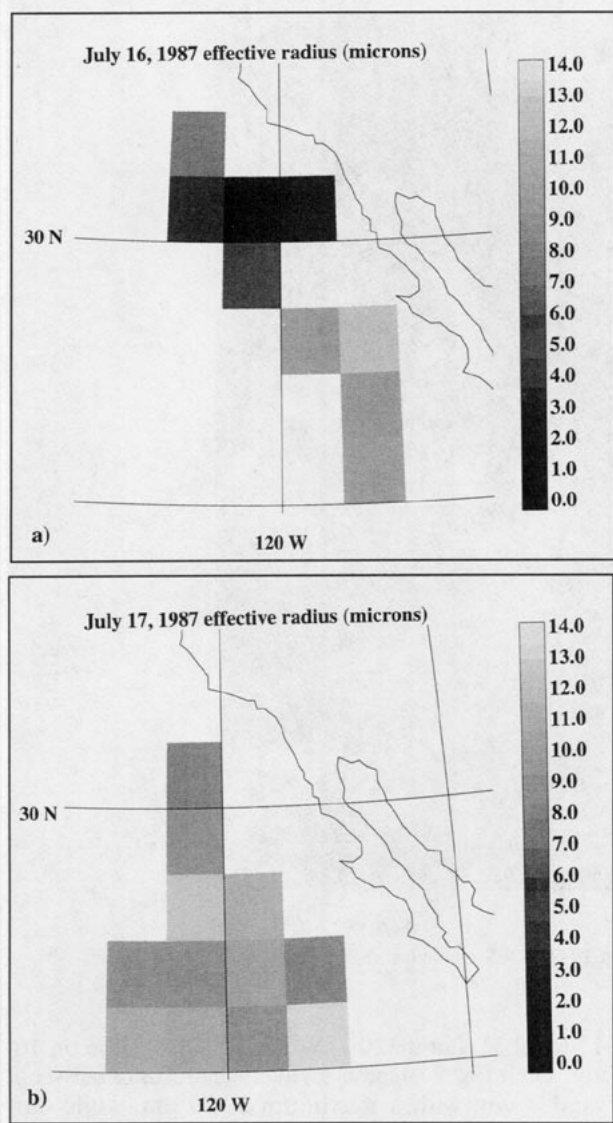


FIG. 14. The derived effective radius over 2.5° by 2.5° grid boxes for (a) 16 July 1987, evening, and (b) 17 July 1987, evening.

odology for retrieving droplet radius is valid, except that ideally LWP variability ought to also be accounted for. When we attempted to extend the application of this methodology to a more general sample of collocated measurements containing high but not necessarily complete cloud cover, we found a reduced dependence of albedo on LWP. We binned the data by collocation event and examined the California data more closely using National Meteorological Center analyses, satellite imagery, and the microwave-retrieved water vapor path values.

These case studies support and extend the conclusions of section 4 but stress the importance of spatial inhomogeneity. Even within stratus regions, significant air mass variability can exist, and often this can be as-

sociated with a particular meteorological situation. The two case studies presented here help illustrate that 1) the methodology is valid when an air mass appears to be homogeneous but that 2) the more common case does involve spatial inhomogeneities, whether they be in cloud morphology or LWP, that play an important role in influencing the large-scale albedo.

Eight collocation events occurred in the California region during our time period of study. In four of these, moist ($WVP > 30 \text{ kg m}^{-2}$) air masses moved southward from the midlatitudes until they intruded into the stratus regions. These air masses generally had higher LWPs and lower albedos than the neighboring cloud decks, and a droplet size cannot be satisfactorily derived. Such a case occurred in August 1987. A contrasting case is that of July 1987, for which the parameterized albedo with a fixed effective radius provides a good fit between the LWP and albedo measurements. In fact, the California data from July 1987 accommodated the best fit to the albedo parameterization of any of the data.

a. July 1987

July may be the month of the year providing the most conducive large-scale physical environment for California stratus cloud development (Klein and Hartmann 1993). Certainly, the conditions present during 16–17 July 1987 confirmed its selection for FIRE. Much of our albedo–LWP data came from these day’s evenings (Fig. 11). The fit made using the Slingo parameterization for an effective radius of $9.3 \mu\text{m}$ is able to explain 83% of the variation in the observations, after grid boxes containing possible precipitation (plotted with an “x”) were excluded from the corre-

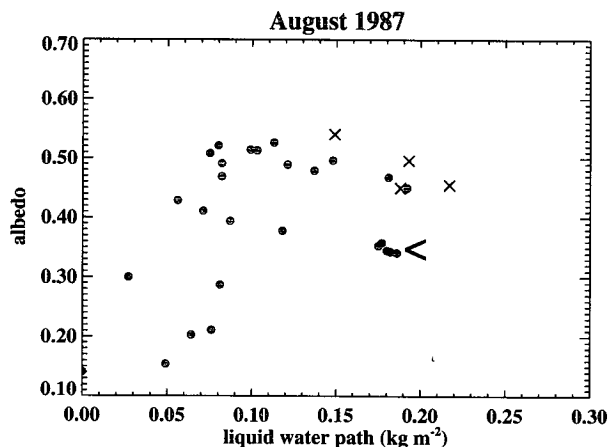


FIG. 15. ERBE albedo versus LWP, California region, August 1987. The × corresponds to grid boxes containing one or more pixels with normalized polarization differences (P) between 0.7 and 0.8. < is pointing to the data from just north of 30°N.

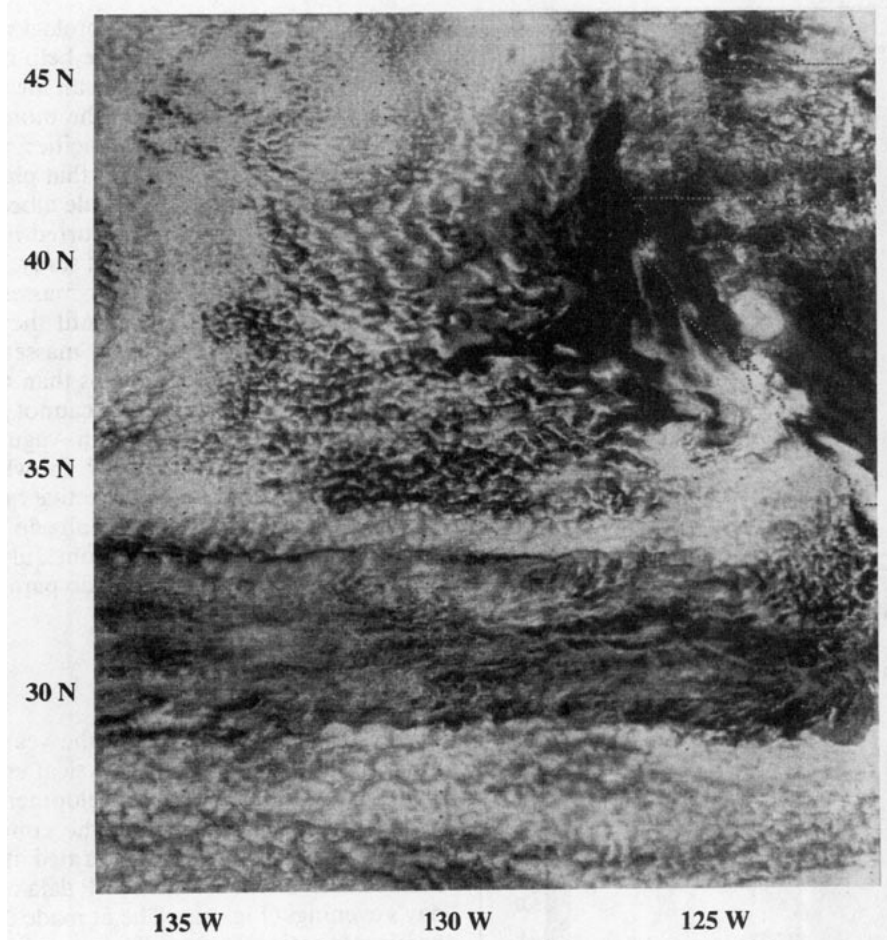


FIG. 16. The 1745 UTC 14 August 1987 GOES visible image.

lation.⁷ A typical 850-mb pressure pattern for these three days (Fig. 12) shows the subtropical high centered near 145°W and 45°N, slightly north of its climatological position for July, and winds within the stratus region are predominantly northerly (Fig. 12). As can be deduced from the visible image (Fig. 13), much of the stratocumulus region was heavily overcast.

The derived radii (Fig. 14) for these grid boxes average $9.3 \pm 3.3 \mu\text{m}$. The effective radii south of 30° tend to be somewhat larger, probably because the clouds are more broken. Young et al. (1992), using a similar technique, found derived radii exceeding $10 \mu\text{m}$ north of 30°N for the morning of 17 July (their Fig. 3c). Nakajima et al. (1991) found larger drops and even drizzle from aircraft data in the area around

31° to 32.5°N and 120.7°W at 1100 local time on 16 July. Their Fig. 8 suggests an average radius of between 7 and $9 \mu\text{m}$, with a maximum at $20 \mu\text{m}$, while our average radius for that area is $3.5 \mu\text{m}$. The difference in the droplet sizes may reflect the different sampling, as drizzle tends to occur on much smaller scales than our grid boxes (Albrecht et al. 1990).

b. August 1987

The large-scale pressure and wind fields for 14–15 August 1987 (not shown) were similar to that for 16–17 July, yet the albedo–LWP scatterplot for the August case shows considerable scatter (Fig. 15). The visible image (Fig. 16) shows a very inhomogeneous cloud field, with a distinct dark strip of about 500 km by 2000 km along 29°–35°N. Figure 17a shows the ERBE albedo image for this case, with the water vapor field overlaid, while Fig. 17b shows the corresponding LWP image, also with the water vapor field overlaid. The dark strip just north of 30°N is seen to have higher values of LWP than neighboring areas, along with a much higher WVP.

⁷ Grid boxes containing pixels with polarization differences between 0.7 and 0.8 tend to have lowered albedos if the mean LWP is low, but not if the mean LWP is high. When the LWP is low, the possible precipitation is probably associated with a low fractional cloudiness, but not so at high LWPs. In this case, the grid boxes containing possible precipitation all came from 19 July.

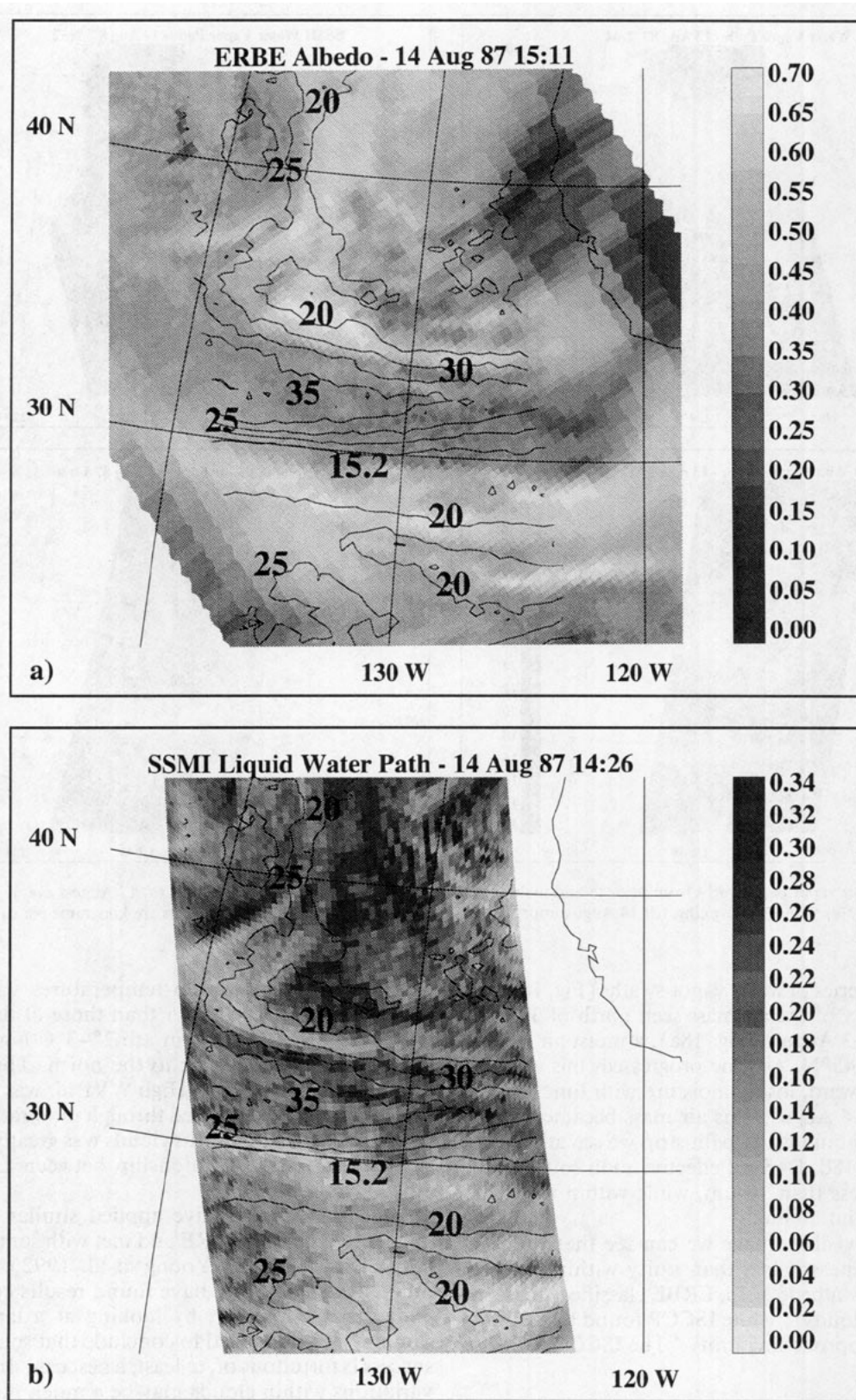


FIG. 17. The 14 August case. (a) The ERBE albedo field (pixel data) with the overlaid water vapor path (WVP) field (kg m^{-2}). (b) the corresponding SSMI LWP (kg m^{-2}) and the same overlaid WVP field.

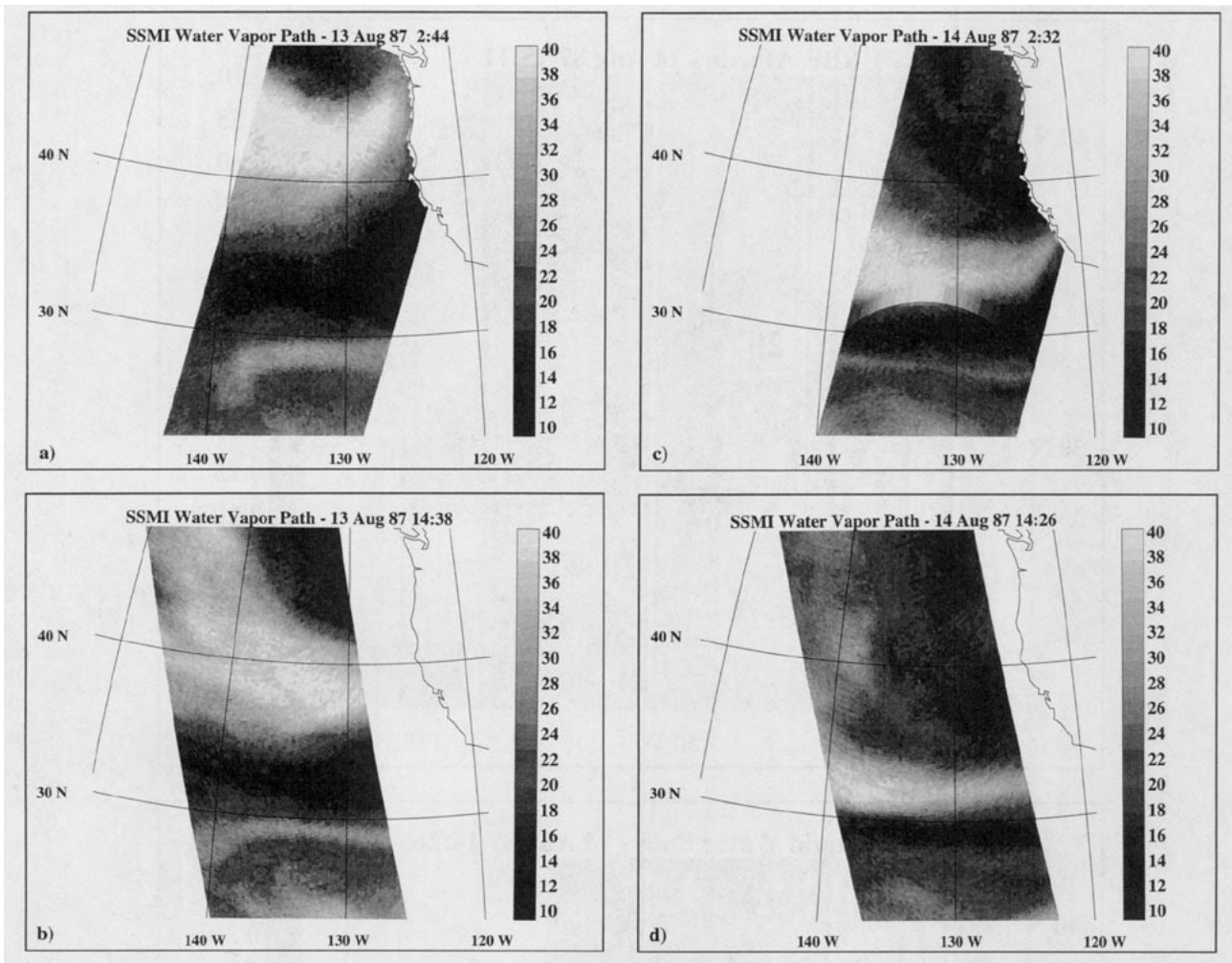


FIG. 18. Water vapor path swaths from prior to and including the 14 August 1987 case. In local time, (a) 12 August evening, (b) 13 August morning, (c) 13 August evening, (d) 14 August morning (coincident with swaths in Fig. 17). Units are kilograms per square meter.

The time series of water vapor swaths (Fig. 18) provides a history of the air mass seen north of 30°N in Fig. 14. On 13 August (Fig. 18a), a moist air mass is seen around 45°N . As time progressed, this air mass moved southward, losing moisture with time. On the morning of 14 August, this air mass became the low albedo–high liquid water path strip we see at 30°N in Figs. 17 and 18d. Derived effective radii south of the swath were less than $10\ \mu\text{m}$, while within the swath they were about $50\ \mu\text{m}$.

From the visible image we can see that the fractional cloudiness is less than unity within the high moisture, low albedo strip. ERBE classified the scene as “mostly cloudy,” while ISCCP found a fractional cloudiness approaching unity.⁸ The ISCCP data also

⁸ ISCCP data from the nearest daytime three-hourly dataset was missing, so we examined ISCCP data from six hours later.

reveal that the cloud-top temperatures within the swath are about 1°C lower than those of the clouds lying to the south of it but are $2^{\circ}\text{--}3^{\circ}\text{C}$ higher than those of the clouds lying to the north. This case is puzzling and interesting. High WVP air was advected southward, and as it passed through the stratus region the character of the stratus clouds was greatly altered. In the process the relationship between LWP and albedo changed.

Other researchers have applied similar methodologies to data from FIRE and met with some success (Minnis et al. 1992; Young et al. 1992). Using a different database, we have found results consistent with theirs. However, by looking at a larger data sample, we are also led to conclude that some of this success is fortuitous or, at least, a best case. Influential variations within clouds may be a much more common feature than the results from FIRE would lead us to believe.

6. Conclusions

Microwave and albedo satellite data from three stratus regions over a total of five seasons (boreal summer and fall only) were collected and applied toward these goals: first, to characterize the regions, and second, to evaluate a satellite methodology for retrieving droplet size and its implications. The data yielded a mean cloud liquid water path of $0.120 \text{ kg m}^{-2} \pm 0.032 \text{ kg m}^{-2}$. The diurnal range in the cloud liquid water is about 25% of the mean LWP. For these cloud LWP values, changes in both cloud LWP or droplet size are important to determining subtropical stratocumulus cloud albedo (see Fig. 1) along with changes in cloud cover.

A positive correlation between cloud liquid water path and cloud amount, apparent in the diurnal cycle and summer to fall changes and in the interregional differences, reinforces the intuitive idea that stratus cloud amount and cloud liquid water path are influenced by the same processes. A relatively strong JJA–SON shift is seen in the Namibian cloud LWPs, and interannual change in the Peruvian stratus LWP coincident with an ENSO episode were evident. Otherwise, interregional differences are small. We found a negative correlation of 0.50 between cloud LWP and low cloud-top temperature, consistent with other studies, and with the interpretation of low CTT as a cloud thickness proxy at timescales larger than a day.

The 84 collocated albedo and LWP measurements for 2.5° by 2.5° completely overcast grid boxes, input into a radiative parameterization, yielded a mean effective radius of $10.1 \pm 4.4 \mu\text{m}$. Throughout the course of the day, the mean effective radius increases, while the mean liquid water path and albedo decrease. The diurnal change in microphysics corroborates the few other observational studies available and may reinforce the importance of entrainment of warm, dry, above-cloud air to droplet spectrum changes.

Aspects of the derivation, along with correlations between LWP, albedo, and droplet size, have important consequences for climate modeling. First, although the range of derived droplet sizes is within the range observed in other studies, the droplet sizes may be overestimated by almost $6 \mu\text{m}$ because of the impact of LWP variability on the average albedo if we rely on the findings of Cahalan et al. (1994b). A related conclusion is then that LWP variability may actually have a more pronounced influence on the albedo, rather than the mean LWP value itself. This is because the modeled albedo is not a strong function of LWP for the range of retrieved mean cloud LWPs. LWP variability can thus have an impact on the average albedo that is equal in magnitude to that of genuine microphysical changes. As we cannot sep-

arate the two effects of droplet size and LWP variability on albedo from each other, either effect can explain the strong negative correlation seen between measured albedo and derived droplet size.

Second, negligible correlation is seen between LWP and effective radius measurements. This reinforces what other researchers have already observed, namely that LWP and droplet size form two independent parameters that must be estimated separately when computing a cloud optical depth. Thus, LWP measurements alone are insufficient for validating parameterizations of the albedo of stratus clouds within climate models.

Neither can cloud droplet size and cloud LWP measurements together adequately validate climate model albedo parameterizations. At the large scale utilized here and by climate models, yet a third parameter, providing some measure of the within-cloud LWP variability, appears to be necessary. This is a direct consequence of the nonlinear relationship between LWP and albedo. One bright note is that such a LWP variability measure does not appear to be required for the smaller 1–8-km scales characteristic of some other satellite resolutions, as evidenced by the results of Han et al. (1994).

Case studies further the main results of this study, namely that the methodology we have tested is valid under conditions of strong spatial homogeneity and, perhaps more importantly, that conditions of spatial inhomogeneity actually occur rather frequently, even within stratus regions. The conditions witnessed during FIRE do not appear to be representative in this regard. The case studies reinforce the need to properly account for this effect within climate models as well. This would include determining how LWP variability relates to cloud fraction, cloud shape (or type), and droplet size and its variability, and also include incorporating those feedbacks into the present climate models.

Acknowledgments. This work was supported by the Earth Radiation Budget Experiment NASA Contract NAS1-18157 and NASA Grant NAGW-3475. Much thanks for prompt and effective technical support goes to Marc Michelsen and Scott Katz. Drs. Grant Petty and Steve Warren provided valuable insight and timely comments throughout the course of this study. We are grateful to the reviewers, the editor Dr. James Coakley, Jr., and Drs. Judy Curry, Conway Leovy, and Brian Mapes for their detailed and well thought out comments, which greatly helped sharpen and clarify the manuscript.

REFERENCES

- Albrecht, B. A., R. W. Barlow, and M. A. Miller, 1990: The large-scale variability in marine stratocumulus defined from aircraft measurements during FIRE. *Conf. Cloud Physics*, San Francisco, CA, Amer. Meteor. Soc., 167–170.

- Alishouse, S., J. Snyder, and R. R. Ferrare, 1990: Determination of cloud liquid water content using the SSM/I. *IEEE Trans. Geosci. Remote Sens.*, **28**, 817–822.
- Baker, M. B., and R. Charlson, 1990: Bistability of CCN concentrations and thermodynamics in the cloud-topped boundary layer. *Nature*, **345**, 142–145.
- Barkstrom, B. R., and G. L. Smith, 1986: The Earth Radiation Budget Experiment: Science and implementation. *Rev. Geophys.*, **24**(2), 379–390.
- Betts, A. K., 1990: Diurnal variation of California coastal stratocumulus from two days of boundary layer soundings. *Tellus*, **42A**, 302–305.
- Bretherton, C. S., 1990: Lagrangian development of a cloud-topped boundary layer in a turbulence closure model. *Conf. Cloud Physics*, San Francisco, CA, Amer. Meteor. Soc., 48–55.
- Cahalan, R. F., W. Ridgway, W. J. Wiscombe, S. Gollmer, and Harshvardhan, 1994a: Independent pixel and Monte Carlo estimates of stratocumulus albedo. *J. Atmos. Sci.*, **51**, 3776–3790.
- , —, —, T. L. Bell, and J. B. Snider, 1994b: The albedo of fractal stratocumulus clouds. *J. Atmos. Sci.*, **51**, 2434–2455.
- Charlson, R. J., J. E. Lovelock, M. O. Andreae, and S. G. Warren, 1987: Oceanic phytoplankton, atmospheric sulphur, cloud albedo and climate. *Nature*, **326**, 655–661.
- Coakley, J. A. Jr., 1991: Reflectivities of uniform and broken layered clouds. *Tellus*, **43B**, 420–443.
- , and T. Kobayashi, 1989: Broken cloud biases in albedo and surface insolation derived from satellite imagery data. *J. Climate*, **2**, 721–730.
- , R. L. Bernstein, and P. A. Durkee, 1987: Effect of ship-stack effluents on cloud reflectivity. *Science*, **237**, 1020–1022.
- Davis, R., 1984: Reflected solar radiances from broken cloud scenes and the interpretation of scanner measurements. *J. Geophys. Res.*, **89**(D1), 1259–1266.
- Duda, D. P., G. L. Stephens, and S. K. Cox, 1989: Microphysical and radiative properties of marine stratocumulus from tethered balloon measurements. *J. Appl. Meteor.*, **30**, 170–186.
- Fairall, C. W., J. E. Hare, and J. B. Snider, 1990: An eight-month sample of marine stratocumulus cloud fraction, albedo, and integrated liquid water. *J. Climate*, **3**, 847–864.
- Goodberlet, M. A., C. T. Swift, and J. C. Wilkerson, 1989: Remote sensing of ocean surface winds with the Special Sensor Microwave/Imager. *J. Geophys. Res.*, **94**, 14 547–14 555.
- Greenwald, T. J., G. L. Stephens, T. H. Vonder Haar, and D. L. Jackson, 1993: A physical retrieval of cloud liquid water over the global oceans using SSM/I observations. *J. Geophys. Res.*, **98**(D10), 18 471–18 488.
- Han, Q., W. B. Rossow, and A. A. Lacis, 1994: Near-global survey of effective droplet radii in liquid water clouds using ISCCP data. *J. Climate*, **7**, 465–497.
- Hanson, H. P., 1991: Marine stratocumulus climatologies. *Int. J. Climatology*, **11**, 147–164.
- Hartmann, D. L., M. E. Ockert-Bell, and M. L. Michelsen, 1992: The effect of cloud type on the earth's energy balance: Global analysis. *J. Climate*, **5**, 1281–1304.
- Heck, P. W., B. J. Byars, and D. F. Young, 1990: A climatology of satellite-derived cloud properties over marine stratocumulus regions. *Seventh Conf. on Atmos. Radiation*, San Francisco, CA, Amer. Meteor. Soc.
- Herman, G. F., and J. A. Curry, 1984: Observational and theoretical studies of solar radiation in arctic stratus clouds. *J. Climate Appl. Meteor.*, **23**, 5–24.
- Hignett, P., 1991: Observations of diurnal variation in a cloud-capped marine boundary layer. *J. Atmos. Sci.*, **48**, 1474–1482.
- Jensen, D. R., 1990: Horizontal variability of the marine boundary layer structure upwind of San Nicolas Island during program FIRE, 1987. *Opt. Eng.*, **29**, 127–130.
- King, M. D., L. F. Radke, and P. V. Hobbs, 1990: Determination of the spectral absorption of solar radiation by marine stratocumulus clouds from airborne measurements within clouds. *J. Atmos. Sci.*, **47**, 894–907.
- Klein, S. A., and D. L. Hartmann, 1993: The seasonal cycle of low stratiform clouds. *J. Climate*, **6**, 1587–1606.
- Kobayashi, T., 1993: Effects due to cloud geometry on biases in the albedo derived from radiance measurements. *J. Climate*, **6**, 120–128.
- Luo, G., X. Lin, and J. A. Coakley, Jr., 1994: 11-Micron emissivities and droplet radii for marine stratocumulus. *J. Geophys. Res.*, **99**(D2), 3685–3698.
- McKee, T. B., and S. T. Cox, 1974: Scattering of visible radiation by finite clouds. *J. Atmos. Sci.*, **31**, 1885–1892.
- Minnis, P., and E. F. Harrison, 1984: Diurnal variability of regional cloud and clear-sky radiative parameters derived from GOES data. Part II: November 1978 cloud distributions. *J. Climate Appl. Meteor.*, **23**, 1012–1031.
- , P. W. Heck, D. F. Young, C. W. Fairall, and J. B. Snider, 1992: Stratocumulus cloud properties derived from simultaneous satellite and island-based instrumentation during FIRE. *J. Appl. Meteor.*, **31**, 317–339.
- Nakajima, T., M. D. King, J. D. Spinhirne, and L. F. Radke, 1991: Determination of the optical thickness and effective particle radius of clouds from reflected solar radiation measurements. Part II: Marine stratocumulus observations. *J. Atmos. Sci.*, **48**, 728–750.
- Nicholls, S., 1984: The dynamics of stratocumulus: Aircraft observations and comparisons with a mixed layer model. *Quart. J. Roy. Meteor. Soc.*, **110**, 783–819.
- , 1987: A model of drizzle growth in warm, turbulent, stratiform clouds. *Quart. J. Roy. Meteor. Soc.*, **113**, 1141–1170.
- Oreopoulos, L., and R. Davies, 1993: Statistical dependence of albedo and cloud cover on sea surface temperature for two tropical marine stratocumulus regions. *J. Climate*, **6**, 2434–2447.
- Petty, G. W., 1990: Observing the marine atmosphere with the special sensor microwave imager. Ph.D. dissertation, University of Washington, 291 pp.
- , 1994: Physical retrievals of over-ocean rain rate from multi-channel microwave imagery. Part I: Theoretical characteristics of normalized polarization and scattering indices. *Meteor. Atmos. Phys.*, **54**, 79–100.
- , and K. B. Katsaros, 1990: Nimbus-7 SMMR precipitation observations calibrated against surface radar during TAMEX. *J. Appl. Meteor.*, **31**, 489–505.
- Radke, L. F., J. A. Coakley Jr., and M. D. King, 1989: Direct and remote sensing observations of the effects of ships on clouds. *Science*, **246**, 1146–1149.
- Rawlins, F., and J. S. Foot, 1990: Remotely sensed measurements of stratocumulus properties during FIRE using the C130 aircraft multichannel radiometer. *J. Atmos. Sci.*, **47**, 2488–2503.
- Ray, P. S., 1972: Broadband complex refractive indices of ice and water. *Appl. Opt.*, **11**, 1836–1843.
- Reynolds, D. W., T. B. McKee, and K. S. Danielson, 1978: Effects of cloud size and cloud particles on satellite-observed reflected brightness. *J. Atmos. Sci.*, **35**, 160–164.
- Rogers, D. P., and L. M. Olsen, 1990: The diurnal variability of marine stratocumulus clouds. *Conf. Cloud Physics*, San Francisco, CA, Amer. Meteor. Soc., J51–J55.
- Rossow, W. B., and R. A. Schiffer, 1991: ISCCP cloud data products. *Bull. Amer. Meteor. Soc.*, **72**, 2–20.
- , and L. C. Garder, 1993: Cloud detection using satellite measurements of infrared and visible radiances for ISCCP. *J. Climate*, **6**, 2341–2369.
- , —, P. Lu, and A. Walker, 1991: International Satellite Cloud Climatology Project (ISCCP) Documentation of Cloud Data. WCRP Rep. WMO/TD-No. 266, 122 pp.

- Slingo, A., 1989: A GCM Parameterization for the shortwave radiative properties of water clouds. *J. Atmos. Sci.*, **46**, 1419–1427.
- , 1990: Sensitivity of the earth's radiation budget to changes in low clouds. *Nature*, **343**, 49–51.
- Smith, G. L., R. N. Green, E. Raschke, L. M. Avis, J. T. Suttles, B. A. Wielicki, and R. Davies, 1986: Inversion methods for satellite studies of the earth's radiation budget: Development of algorithms for the ERBE mission. *Rev. Geophys.*, **24**(2), 407–421.
- Stephens, G. L., 1984: The parameterization of radiation for numerical weather prediction and climate models. *Mon. Wea. Rev.*, **112**, 826–867.
- Suttles, J. T., R. N. Green, P. Minnis, G. L. Smith, W. F. Staylor, B. A. Wielicki, I. J. Walker, D. F. Young, V. R. Taylor, and L. L. Stowe, 1988: Angular radiation models for earth-atmosphere system. Vol. 1—Shortwave radiation. NASA Ref. Pub. 1184, 144 pp.
- Taylor, V. R., and L. Stowe, 1984: Reflectance characteristics of uniform earth and cloud surfaces derived from Nimbus-7 ERB. *J. Geophys. Res.*, **89**(D4), 4987–4996.
- , and ———, 1986: Revised reflectance and emission models from Nimbus-7 ERB Data. *Sixth Conf. on Atmospheric Radiation*, Williamsburg, VA, Amer. Meteor. Soc., J19–J22.
- Thompson, S. L., and E. J. Barron, 1981: Creteaceous and present earth albedos. *J. Geology*, **89**, 143–164.
- Warren, S. G., C. J. Hahn, J. London, R. M. Chervin, and R. L. Jenne, 1988: Global distribution of total cloud cover and cloud type amounts over the ocean. NCAR Tech. Notes TN-317+STR or DOE/ER-0406.
- Welch, R. M., and B. A. Wielicki, 1984: Stratocumulus cloud field reflected fluxes: The effect of cloud shape. *J. Atmos. Sci.*, **41**, 3085–3103.
- Wentz, F. J., 1991a: Users's Manual SSM/I Antenna Temperature Tapes, Rev 1. RSS Tech. Rep. 120191, Remote Sensing Systems, Santa Rosa, CA.
- , 1991b: Measurement of Oceanic Wind Vector Using Satellite Microwave radiometers. RSS Tech. Rep. 051591, Remote Sensing Systems, Santa Rosa, CA.
- Wielicki, B. A., and R. N. Green, 1989: Cloud identification for ERBE radiative flux retrieval. *J. Appl. Meteor.*, **28**, 1133–1146.
- , and L. Parker, 1992: On the determination of cloud cover from satellite sensors: The effect of sensor spatial resolution. *J. Geophys. Res.*, **97**(D12), 12 799–12 823.
- Wiscombe, W. J., R. M. Welch, and W. D. Hall, 1984: The effects of very large drops on cloud absorption. Part I: Parcel models. *J. Atmos. Sci.*, **41**, 1336–1355.
- Woodruff, S. D., R. J. Slutz, R. L. Jenne, and P. M. Steurer, 1987: A Comprehensive Ocean-Atmosphere Data Set. *Bull. Amer. Meteor. Soc.*, **68**, 1239–1250.
- Young, D. F., P. Minnis, K. Katsaros, A. Dybbroe, and J. Mileta, 1992: Comparison of techniques for deriving water-cloud microphysical properties from multiple satellite data. *11th Int. Conf. on Clouds and Precipitation*. Montreal, Quebec, Canada, 1053–1056.